Journal of Marine Science and Technology

Volume 26 | Issue 6 Article 7

VORTEX MOTIONS AROUND A VERTICALLY VIBRATING CYLINDER IN OSCILLATORY FLOWS

Symphony Chakraborty
Department of Mechanical Engineering, National Taiwan University of Science and Technology, Taipei, Taiwan, R.O.C

Tzu-Wen Lin
Department of Mechanical Engineering, National Taiwan University of Science and Technology, Taipei, Taiwan, R.O.C

Ming-Jyh Chern
Department of Mechanical Engineering, National Taiwan University of Science and Technology, Taipei, Taiwan, R.O.C

VORTEX MOTIONS AROUND A VERTICALLY VIBRATING CYLINDER IN OSCILLATORY FLOWS

Acknowledgements

The authors would like to express their gratitude for the financial support from the Ministry of Science and Technology, Taiwan (Grant No: MOST 103-2212-E-011-110-MY3 and MOST 106-2221-E-011-079).

Journal of Marine Science and Technology, Vol. 26, No. 6, pp. 826-837 (2018)
DOI: 10.6119/JMST.201812_26(6).0007

VORTEX MOTIONS AROUND A VERTICALLY VIBRATING CYLINDER IN OSCILLATORY FLOWS

Symphony Chakraborty, Tzu-Wen Lin, and Ming-Jyh Chern

Key words: direct-forcing immersed boundary method, lock-in phenomenon, vortex-induced vibration, springing.

ABSTRACT

Numerical simulations of the vortex-induced vibration (VIV) on a circular cylinder in an oscillatory flow were conducted using the direct-forcing immersed boundary (DFIB) method. VIV of structures is a practical engineering problem. Many engineers have devoted themselves to research on the prevention of VIV, which can cause severe damage to offshore construction equipment and structures. Fluctuating hydrodynamic force induces vibration of structures because of the vortex around the structure. This vibration causes structural failure due to the lock-in phenomenon. A phenomenon termed "springing" (a second-order wave effect caused by superposition of the incident waves and the reflected waves or other wave systems) was also observed in this study. This phenomenon is more hazardous than the lock-in phenomenon because it causes a very high transverse frequency response that can result in serious structural damage. In springing, a vortex that is bounded near the cylinder appears; this vortex is termed a "bound vortex." A stationary cylinder in oscillatory flow was used to so that the experimental and numerical results of the dynamic and velocity components at three cross-sectional areas could be verified and validated with published results. The DFIB method was then applied to simulate a moving circular cylinder in the transverse direction in an oscillatory flow with varying mass loading. The results of the varying mass ratio were discussed as well as the effects of the reduced velocity, and the corresponding lock-in region was determined. This proposed model can be used for predicting VIV of structures.

I. INTRODUCTION

Vortex-induced vibration (VIV) is a great concern in many engineering fields, such as marine, civil, wind, and aerospace engineering, and it is of particular relevance to renewable energy projects, which have become increasingly common. Engineers have been trying to prevent the VIV phenomenon in offshore equipment, which causes structural resonance and serious damage to equipment. When fluid flows through a structure, the surrounding vortex shedding causes the original hydrodynamics to change over time, because the vortex is alternatively shed up and down. This movement causes self-excited vibration of the structure. When the hydrodynamic frequency and natural frequency of objects are similar, high amplitude is produced, resulting in the lock-in phenomenon.

Recently, interest has grown in identifying nonlinear mechanisms that induce springing or ringing in complex offshore structural systems. The springing and ringing phenomena have been reported by Gurley and Kareem (1998). Vibration caused by springing and ringing is more servere than the lock-in phenomena and can cause structural damage. Springing is a high-frequency response in the vertical and bending modes of tension leg platforms (TLPs) and gravity-based structures that occurs because of the second-order wave effects at the sum frequencies. However, ringing is a rare event and was unaccounted for in standard response analysis codes until recent experimental and full-scale observations uncovered it. Higher-order loading mechanisms lead to the onset of ringing. In recent years, considerable interest has grown in determining nonlinear mechanisms that cause ringing in complex maritime structural systems. The peak of transient frequency response has been observed in offshore systems, specifically in TLPs. The effect of ringing on the fatigue life of TLP tendons should be considered in the overall response assessment. Because lock-in, springing, and ringing may occur due to the interaction of waves with structures, investigating vibration in a structure in oscillatory flow, which is the primary motion in waves or tidal currents, is worthwhile. However, predicting structural vibration in oscillatory flow is challenging. One of the difficulties is identifying the condition that induced the phenomena. Numerous parameters must be examined to identify thee condition. Moreover, if a numerical approach is used, then a scheme to estimate the vibration caused by those phenomena is required.

Interaction between a cylinder and oscillatory flow has attracted considerable research interest. Sumer and Fredsøe (1988) presented the transverse vibrations on an elastically mounted rigid cylinder exposed to an oscillatory flow with the Keulegan-Carpenter

Paper submitted 08/29/17; revised 07/25/18; accepted 11/27/18. Author for correspondence: Ming-Jyh Chern (e-mail: mjchern@mail.ntust.edu.tw).
Department of Mechanical Engineering, National Taiwan University of Science and Technology, Taipei, Taiwan, R.O.C.

(*KC*) number varying from 5 to 100. The reduced velocity U_R^* varied in the range of 0-16 in most cases. They considered different combinations of spring stiffness and cylinder mass before finally obtaining the responses of the cylinder based on the *KC* number and U_R^*. Kozakiewicz et al. (1992) studied the transverse vibration of a cylinder near the wall in an oscillatory flow at three different *KC* numbers (*KC* = 6, 20, and 65). Moreover, Kozakiewicz et al. (1996) studied the vortex flow around a freely vibrating circular cylinder in an oscillatory flow, specifically in the lock-in regions. In their experiments, vortices in the flow were visualized using aluminum-powder technology. Variations in the vortex motion were discussed with respect to the vortex influence on the lift force.

Dütsch et al. (1998) conducted experiments to study variation in the velocity of a moving cylinder in an oscillatory flow at low Reynolds numbers *Re* and low *KC* numbers. They considered three cases with different combinations of *Re* and *KC* numbers—*Re* = 100 and *KC* = 5, *Re* = 200 and *KC* = 10, and *Re* = 210 and *KC* = 6. They found good agreement between the experimental results and corresponding numerical flow predictions. Zhao et al. (2012) studied the movement of a cylinder in the cross-flow direction of an oscillatory flow. The simulations were conducted at KC = 10 and 20. The reduced velocity U_R^* varied from 1 to 36, and the frequency response was found to contain only one harmonic when U_R^* was less than eight for both *KC* numbers. When U_R^* was greater than eight, the frequency response contained multiple harmonics. Moreover, for different values of U_R^*, the vibration frequency mode changed from one regular harmonic to another.

Chern et al. (2013) proposed the direct-forcing immersed boundary (DFIB) method to study the interaction between an oscillatory flow and a single cylinder at *KC* = 2-10, and they used an established numerical model for further simulation of oscillatory flows around four cylinders set in a square arrangement at different parameter values. The results revealed that a higher number of vortices occur at high *KC* numbers. However, when the oscillatory flow direction was changed to a 45° angle of attack, the flow pattern was symmetric at *KC* = 5. This result is different from the result of the case in which the cylinders were in a uniform flow. A comparison of C_f and C_l for the horizontal and oblique oscillatory flows revealed that C_f was not affected by the flow direction, whereas C_l reduced at *KC* = 5. Moreover, in the oblique oscillatory flow, C_l on the second and the third cylinder was larger than that on the first and fourth cylinder.

Zhao et al. (2013) numerically studied the two-degrees-of-freedom vortex-induced vibration of a circular cylinder in an oscillatory flow. Simulations were conducted at *KC* = 10, 20, and 40, and U_R^* varied from 1 to 30. The focus of their study was to investigate the relationship between the vibration frequency, vortex shedding mode, hydrodynamic force, and response of the circular cylinder. They found that the frequency mode of the vibration was not only based on the *KC* number but also on U_R^*. By analyzing the vortex shedding, they concluded that the vibration frequency normalized by the frequency of the oscillatory flow equaled the number of the vortex pairs that were shed from the cylinder.

Fu et al. (2014) researched the characteristics of vortex vibrations in an oscillatory flow. The results revealed that the VIV in the oscillatory flow was markedly different from that in the uniform flow. Features such as intermittent VIV, hysteresis, amplitude modulation, and mode conversion were observed. VIV development processes caused by various phenomena in the oscillatory flow, including build-up, lock-in, and dying-out phenomena, were proposed and analyzed.

Chern et al. (2016) simulated the hydroelastic behavior of a rigid horizontal circular cylinder in regular progressive waves, and the parameters were fixed at the following values: *Re* = 110, *KC* = 10, and reduced velocity varied in the range of $4.5 < U_R^* < 5.3$. They successfully explored three transverse vibration regimes: lower beating ($4 < U_R^* < 4.5$); lock-in ($4.7 < U_R^* < 4.8$); and upper beating ($5 < U_R^* < 10$) modes. Recent years have seen growth in the use of the immersed boundary method for simulating the complex fluid–structure interaction (FSI) problem. To overcome this FSI problem, the DFIB method that mainly involves the interaction between the virtual forces of a fluid and solud in the Navier-Stokes equations to express fluid-solid coupling was used. The major advantage of the DFIB method is that it has less computational cost than the conventional body-fitted method when simulating moving boundaries. Sotiropoulos and Yang (2014) noted that the immersed boundary method is difficult to apply to rigid body problems because of the numerical instabilities associated with stiff systems that are inherent to rigid bodies. To help resolve problems in complex flow simulations, the hybrid Cartesian-immersed boundary method was proposed by Mohd-Yusof (1996), who noted that the immersed boundary method is based on curvilinear background grids. This method has achieved considerable academic attention, for example in the studies by Chern et al. (2013) and Shen et al. (2009).

The present study sought to use the DFIB method to simulate the vibration on a cylinder in an oscillatory flow generated by a vortex motion. To observe the effect of different U_R^* values in the vortex motion for different values of mass ratio m^*, the flow variations were examined in this study. This paper is arranged as follows. In section II, the governing equations and numerical procedures are explained, and the proposed numerical model is validated. In section III, the influence of reduced velocity and mass ratio on the cylinder, the vortex patterns, and transverse displacement are discussed. Moreover, the corresponding frequencies at which the springing and lock-in phenomena occur are identified. Finally, the conclusions are presented in section IV.

II. MATHEMATICAL FORMULAS AND NUMERICAL MODEL

The DFIB method and the finite volume method were utilized

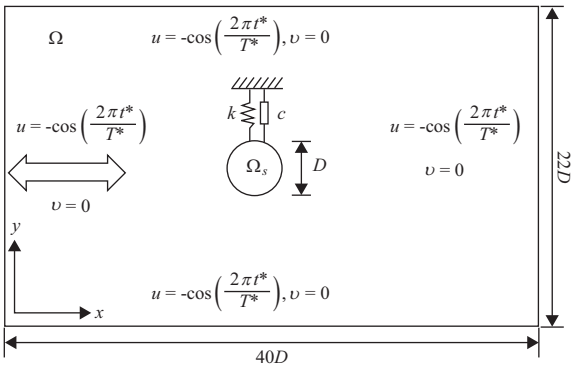

Fig. 1. Schematic of a moving circular cylinder in an oscillatory flow.

to establish the proposed numerical model for simulating the interaction between a circular cylinder and an oscillatory flow. The basic principle of the DFIB method is to add a virtual force in the incompressible Navier-Stokes equation, and then, the effect of solid is considered in the fluid domain. This method reduces the computational time for mesh generation for a complex solid geometry. The governing equations for the interaction of fluids and solids and the details of the proposed numerical method are explained as follows.

1. Governing Equations

Fig. 1 displays a schematic of a vibrating circular cylinder in an oscillatory flow. A virtual spring is considered to restrict the movement of the cylinder in the transverse direction. An incompressible viscous fluid is considered in this problem. The dimensionless governing equations for mass and momentum conservation are described as follows:

$$\nabla \cdot \mathbf{u} = 0, \quad \text{in } \Omega, \tag{1}$$

and

$$\frac{\partial \mathbf{u}}{\partial t^*} + \nabla \cdot (\mathbf{uu}) = -\nabla p + \frac{1}{Re}\nabla^2 \mathbf{u} + \mathbf{f}^*, \text{ in } \Omega, \tag{2}$$

where **u** is the dimensionless velocity that is nondimensionalized by the inlet free stream velocity U_∞; p is the dimensionless pressure; t^* is the dimensionless time defined by tU_∞/D, where D represents the diameter of the cylinder; Re is the Reynolds number defined by DU_∞/v; v is the kinematic viscosity of the fluid; and $\mathbf{f}^*$ is the dimensionless virtual force defined as fD/U_∞^2. Eqs. (1) and (2) are discretized using the finite volume technique. The third-order Adam-Bashforth method is used to discretize the temporal derivative in Eq. (2). The diffusion and convection terms in Eq. (2) are discretized using the second-order central difference method and the QUICK scheme proposed by Leonard (1979), respectively. The projection method proposed by Chorin (1967) is adopted for solving the pressure field. The proposed method has been used for a number of benchmark tests, such as those published in the studies by Chern et al. (2014) and Chern et al. (2015).

2. Equation of the Cylinder Motion

The cylinder moves because the hydrodynamic force caused by vortex shedding is exerted on the cylinder. Conversely, the movement of the cylinder is restricted by the virtual spring. This vibration can be considered a type of forced vibration, which can be described using Newton's second law of motion. Given that the cylinder is rigid, the dimensionless governing equation of the cylinder movement is described as follows:

$$\ddot{Y} + \frac{4\pi\zeta}{U_R^*}\dot{Y} + \left(\frac{2\pi}{U_R^*}\right)^2 Y = \frac{2C_L(t^*)}{\pi m^*}, \tag{3}$$

where $\ddot{Y}$, $\dot{Y}$, and Y represent the normalized transverse acceleration, velocity, and displacement of the center of the rigid circular cylinder, respectively. The dimensionless displacement Y is defined as $\frac{d_y}{D}$, where d_y is the displacement of the cylinder center in the y direction; U_R^* is the reduced velocity of the system defined as $\frac{U_\infty}{f_n D}$, where f_n is the natural frequency of the solid body; and ζ is the structural damping ratio defined as $\frac{c}{2\sqrt{m_s k}}$, where c is the structural damping, m_s is the solid mass per unit length, and k is the structural stiffness. The term m^* is the mass ratio of the solid to liquid mass and is defined as $\frac{4m_s}{\pi\rho_f D^2}$, whereas $C_L(t^*)$ is the instantaneous lift coefficient. The instant C_L is calculated by the DFIB method at each time step and is considered as the external force in Eq. (3). The fourth order Runge-Kutta algorithm is then used to solve Eq. (3). Consequently, the displacement of the cylinder center is predicted.

3. DFIB Method

To calculate the interaction between a fluid and the vibrating cylinder, the DFIB method proposed by Mohd-Yusof (1996) was adopted in the present study. Due to the movement of the cylinder and its geometry, the mesh used was a nonuniform Cartesian grid. As more grids cluster near the cylinder, the calculation accuracy of the cylinder movement increases. This mesh does not have to be generated at each time step; thus, it is more efficient than the body-fitted mesh. Details of the proposed DFIB method are described as follows.

1) Calculation of the Virtual Force

The dimensionless force term $\mathbf{f}^*$ in Eq. (2) is defined by the difference between the intermediated velocity $\mathbf{u_f}$ and the solid velocity $\mathbf{u}_s$ at each cell, that is,

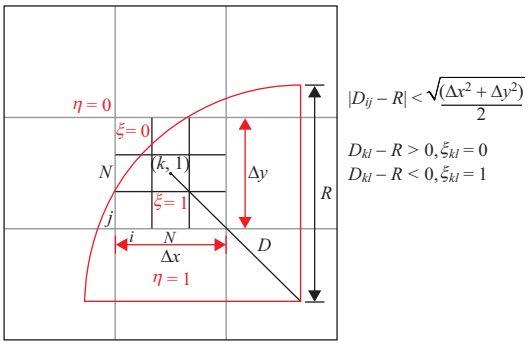

(a) Volume of solid function

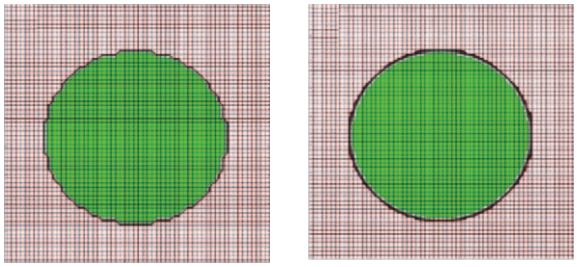

(b) η contours without subgrids (c) η contours with subgrids

Fig. 2. Subgrids (100 × 100) using ξ to redefine the solid and fluid regions.

$$\mathbf{f}^* = \eta \frac{\mathbf{u}_s - \mathbf{u}_\mathbf{f}}{\Delta t}, \text{ in } \Omega_s, \tag{4}$$

where $\mathbf{u}_s$ is the velocity of the solid cylinder center and η is defined as the volume fraction of the solid in a computational cell. The function η is defined to be 1 and 0 for the solid and fluid cells, respectively. For a circular cylinder, the indicator function η is determined using the following:

$$\eta(x, y, t) = \begin{cases} 1, & (x - x_c(t))^2 + (y - y_c(t))^2 \le R^2 \\ 0, & (x - x_c(t))^2 + (y - y_c(t))^2 > R^2 \end{cases}, \tag{5}$$

where R is the radius of the cylinder; (x, y) are the coordinates of the center of the computational cell; and (x_c, y_c) are the coordinates of the center of the cylinder. For a cell with a solid-fluid interface, η varies between 0 and 1 because it is not a fully solid cell. The so-called subgrid method that allocates more cells in the boundary cell is used. Once a cell identified as a boundary cell, more cells are used to refine the boundary cell. Another volume value of the solid function ξ is determined using Eq. (5) for each cell. Subsequently, η at this boundary cell is determined using Eq. (6),

$$\eta_{i,j} = \frac{\sum \xi_{k,l}}{N \times N}, \tag{6}$$

where $N \times N$ cells are used to fulfill the boundary cell. If N is sufficiently large, the solid-fluid interface can be represented by a smooth curve, and η will be more accurate. Fig. 2(a) shows that ξ is 0 and 1 in the fluid and solid cells, respectively. If the distance between the center of the cylinder and the center of the subgrid is less than the radius of the cylinder, ξ will be 1. Conversely, ξ is 0 when the distance is greater than the radius. Fig. 2(c) presents the distribution of η by using the subgrid technique. The distribution of η with the improvement of the subgrid approach is smoother compared with the distribution without the improvement, as shown in Fig. 2(b).

2) Numerical Methods for Solving the Navier-Stokes Equations

The momentum equation, Eq. (2), uses a three-step time-split scheme to advance the flow field (Chorin, 1967). First, the intermediate velocity $\mathbf{u}'$ is calculated by solving the convection-diffusion equation without a pressure gradient and virtual force term at the beginning of each time step.

$$\frac{\mathbf{u}' - \mathbf{u}^n}{\Delta t^*} = S^n, \tag{7}$$

where S^n includes the convective and diffusive terms in Eq. (2).

In the second step, $\mathbf{u}'$ is marched to the second intermediate velocity $\mathbf{u}''$ by incorporating the pressure gradient term

$$\frac{\mathbf{u}'' - \mathbf{u}'}{\Delta t^*} = -\nabla p^{n+1}. \tag{8}$$

By taking divergence for both sides of Eq. (8), we obtain the following:

$$\frac{\nabla \cdot \mathbf{u}'' - \nabla \cdot \mathbf{u}'}{\Delta t^*} = -\nabla^2 p^{n+1}. \tag{9}$$

However, the second intermediate velocity $\mathbf{u}''$ should satisfy the mass conservation presented in Eq. (1). Then, Eq. (9) provides Poisson's equation of pressure.

$$\nabla^2 p^{n+1} = \frac{1}{\Delta t^*} \nabla \cdot \mathbf{u}'. \tag{10}$$

After solving Eq. (10), the second intermediate velocity $\mathbf{u}''$ can be determined using Eq. (8).

Finally, the virtual force term that represents the effect of a solid body on fluid should be included in the third step so that the final velocity $\mathbf{u}^{n+1}$ can be obtained by adding the virtual force term as follows:

$$\frac{\mathbf{u}^{n+1} - \mathbf{u}''}{\Delta t^*} = \mathbf{f}^{*n+1}. \tag{11}$$

Here, $\mathbf{f}^{*n+1}$ refers to a force to hold or drive a solid body when it is at rest or moves, and it is calculated by the rate of momen-

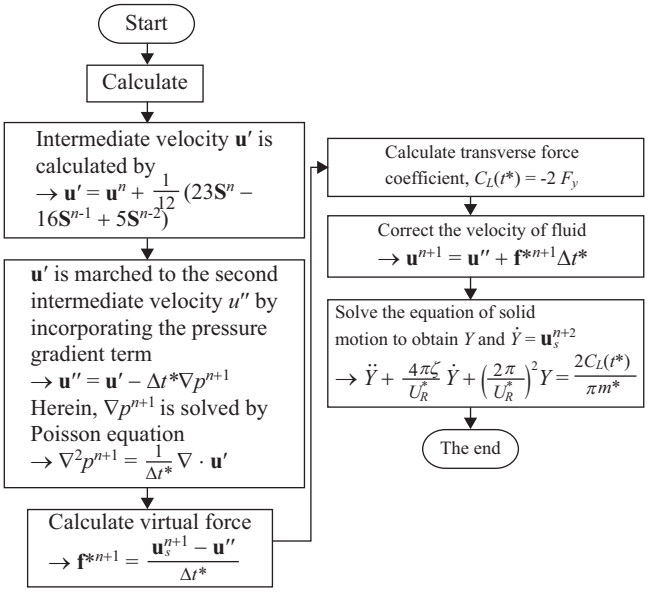

Fig. 3. Flowchart of the numerical procedures.

tum change of a solid body and is proportional to the difference between the solid velocity at the $n + 1^{th}$ time step and the local fluid velocity at the second step. To satisfy the no-slip boundary conditions at the fluid-solid interface, it is crucial to ensure that the fluid velocity $\mathbf{u}^{n+1}$ equals the solid speed $\mathbf{u}_s^{n+1}$. Thus, we obtain the following equation:

$$\mathbf{f}^{*n+1} = \eta \frac{\mathbf{u}^{n+1} - \mathbf{u}''}{\Delta t^*} = \eta \frac{\mathbf{u}_s^{n+1} - \mathbf{u}''}{\Delta t^*}. \tag{12}$$

As a vibrating circular cylinder is the object considered in this study, the solid velocity $\mathbf{u}_s$ in the transverse direction can be determined using Eq. (3). The external hydrodynamic force **F** is determined by the integral of the virtual force over the solid body (Chern et al., 2015). That is,

$$\mathbf{F} = \iiint_{\Omega} \mathbf{f}^* \mathrm{d}V, \tag{13}$$

where **F** is the resultant total hydrodynamic force. In the proposed model, Simpson's 1/3 rule is used to calculate the integral of the virtual force over the cylinder. The transverse force coefficient C_L can be calculated using the following equation

$$C_L = -2F_y. \tag{14}$$

C_L is then employed in Eq. (3) to determine $\mathbf{u}_s$ in the next time step. Details of the algorithm of the fluid-structure interaction at each time step are displayed in Fig. 3.

4. Oscillatory Flow Boundary Condition

As an oscillatory flow is considered in this study, the instantaneous velocity boundary conditions are applied to the four boundaries of the computational domain. The dimensionless velocity components of the oscillatory flow vary based on the following equation:

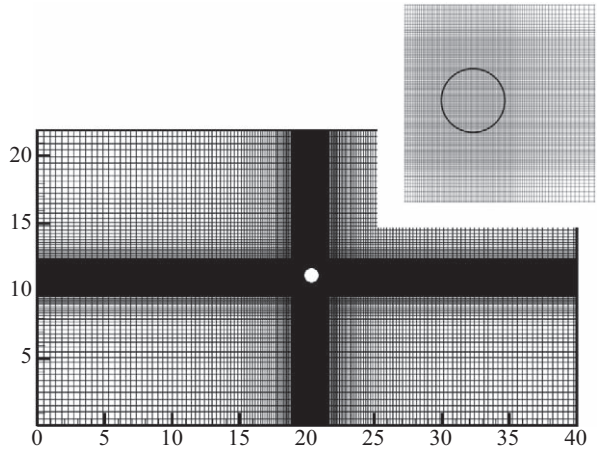

Fig. 4. Grid configuration of a freely vibrating circular cylinder for transverse vibrations.

$$u = -\cos\left(\frac{2\pi t^*}{T^*}\right) \text{ and } v = 0, \tag{15}$$

where T is expressed as the period of the oscillatory flow.

5. Verification of the DFIB Model

1) Computational Domain and Computation Time

The grid generation and computational mesh around the transverse vibrating cylinder are presented in Fig. 4. The computational domain of $40D \times 22D$ is discretized into 239 × 169 nonuniform Cartesian grids. The purpose of using a nonuniform grid configuration is to increase the accuracy of the present method and to accurately capture the VIV phenomenon. The time increment $\Delta t^*$is set at 10^{-3} to satisfy the Courant-Friedrichs-Lewy (CFL) number of 0.04. Here, the CFL number defined as $\left(\frac{u\Delta t}{\Delta x} + \frac{v\Delta t}{\Delta y}\right)$ is always less than 0.1. Moreover, the convergence criterion D is 10^{-2} for the maximum mass residual considered in this study. The longest simulation requires approximately 25 days, which corresponds to the dimensionless time t^* of 1200. A PC cluster consisting of an Intel Xeon CPU E31275 at 3.40 GHz was used to conduct the numerical simulations.

2) Grid Independence and Validation of In-House Numerical Code

Several grid configurations were utilized to simulate the transverse oscillations of a circular cylinder to ensure that the numerical results were grid independent. In the grid independent study, the flow and structural parameters were selected based on a study by Leontini et al. (2006) with the following parameters: $Re = 200$, $m^* = 10$, $\zeta = 0.01$, and $U_R^* = 3.5$. Four grids) 151 × 131, 185 × 165, 239 × 169, and 249 × 185 were considered

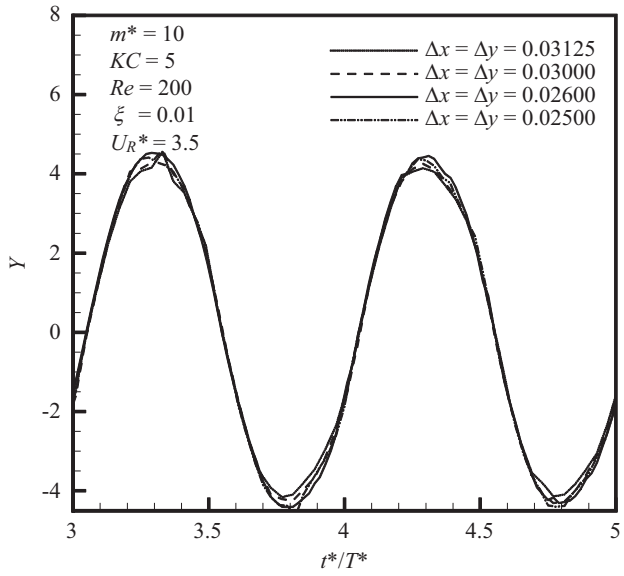

Fig. 5. Grid independence test: time history of the transverse motions of the cylinder.

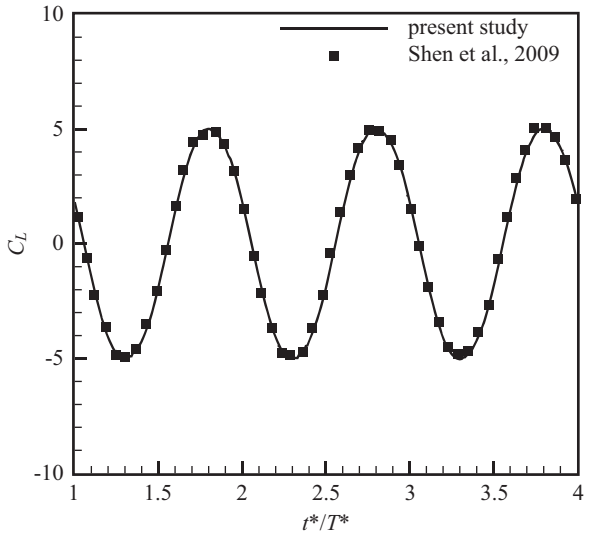

Fig. 6. Time histories of C_L with a stationary circular cylinder.

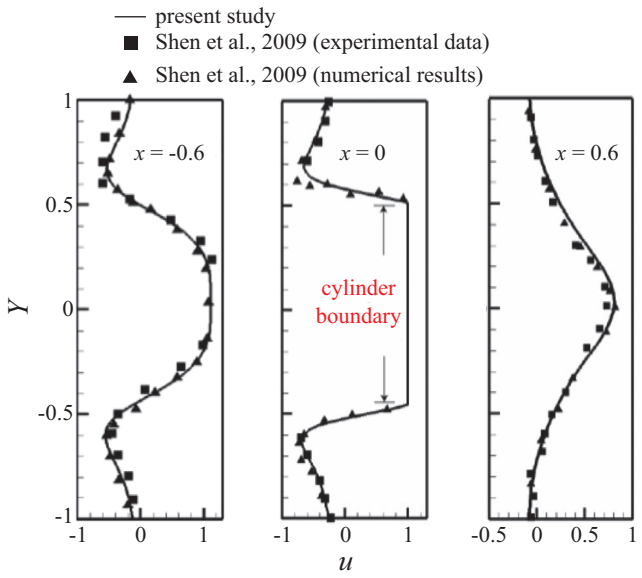

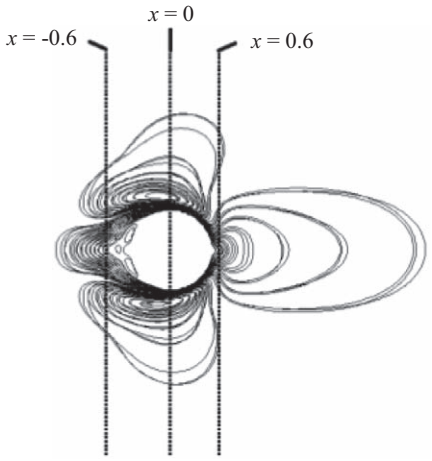

Fig. 7. Comparison of the velocity components at three different cross-sections at time *t equal to* n · *T* + *T*/2.

in this study. The corresponding smallest grid spacing of these meshes were 0.03125*D*, 0.03*D*, 0.026*D*, and 0.025*D*, respectively, for the grids clustered in the vicinity of the cylinder. Therefore, to increase the accuracy of the numerical results and reduce the computation time, Δx and Δy value of 0.026 were chosen to obtain more accurate and consistent results, as presented in Fig. 5. We also selected this grid for the other cases subsequently discussed. The cylinder was located in the middle of the calculation domain. To verify the proposed numerical model, for the flow condition, *KC* and *Re* were set to 5 and 100, respectively, to simulate the oscillatory flow through a single fixed cylinder. Numerical predictions of the hydrodynamic coefficients and horizontal velocity components were plotted in three different cross-sections. Fig. 6 presents the time history of the force coefficient at *KC* = 5 As shown, the numerical results obtained using a body-fitted coordinate system by Shen et al. (2009) agree with the results of the present study. The oscillatory flow was also verified using a single vibrating cylinder at the following parameter values: *KC* = 10 and *Re* = 110. Fig. 7 illustrates the predicted horizontal velocity profiles at three sections with *x* = -0.6, 0, and 0.6 at the phase time t of $n \cdot T + T/2$. The experimental measurements and numerical results reported by Shen et al. (2009) agree with the present numerical predictions. This reveals the capability of the used DFIB scheme.

The DFIB model was also compared with the work of Sumer and Fredsøe (1988) for oscillatory flow at *KC* = 10 and *Re* = 110. The variation in the dimensionless natural frequency $\frac{f}{f_n}$ with respect to the reduced velocity U_R^* is presented in Fig. 8. The results of the present study are in good agreement with

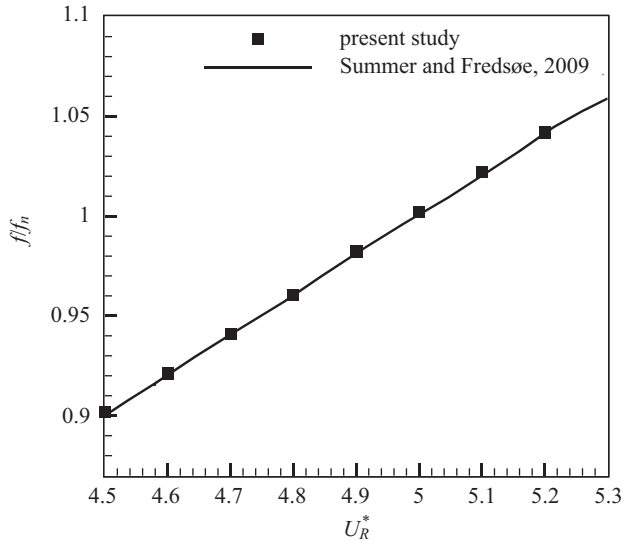

Fig. 8. Variation in nondimensional frequency with reduced velocity.

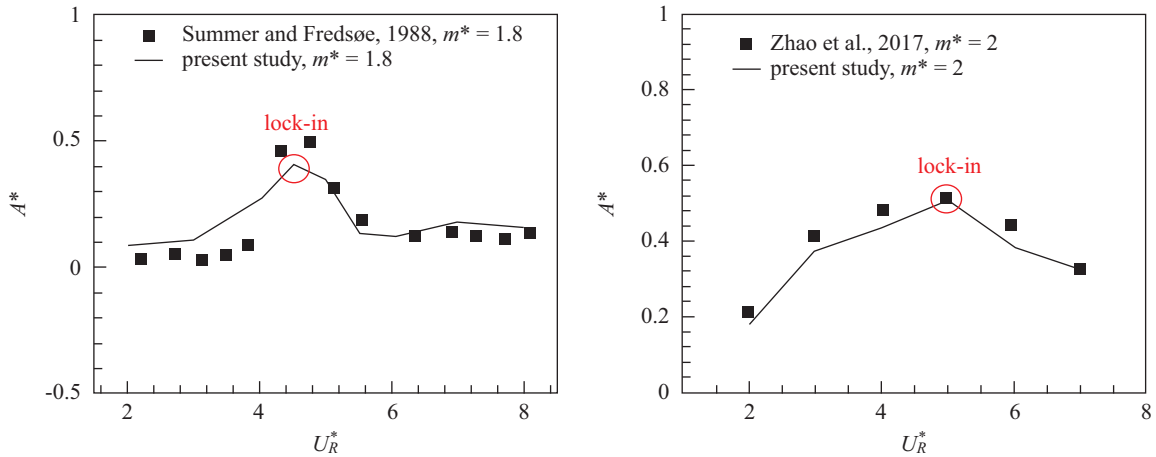

Fig. 9. Comparison of amplitude and frequency response of numerical results.

those of Sumer and Fredsøe. Fig. 9(b) presents the variations in the response amplitude and frequency with U_R^* for mass ratio $m^* = 2$. The experimental and numerical results of the present study agree with those of the study by Zhao et al. (2017). However, a discrepancy is found in Fig. 9(a). The discrepancy is because Sumer and Fredsøe (1988) considered a stationary cylinder in turbulent flow ($Re = 20{,}000$), whereas the present study is based on the transverse motion of a cylinder in laminar flow at $Re = 500$. From the aforementioned results, the proposed model can simulate the interaction between an oscillatory flow and a single cylinder.

III. RESULTS AND DISCUSSIONS

It is known that VIV on an elastically mounted circular cylinder is effected by a group of parameters, including mass ratio (m^*), reduced velocity (U_R^*), structural damping ratio (ζ), and Reynolds number (Re). The effect of varying the reduced velocity U_R^* was investigated in this study. Cylinder vibration is a direct consequence of exerting hydrodynamic force on a solid body in a fluid flow. Therefore, an accurate prediction of the flow field and hydrodynamic forces applied to solids is the most crucial factor in VIV simulation. To predict the response of a vibrating cylinder, a circular cylinder that vibrates only in the transverse direction of oscillatory flow was used as an example. The results and various effects of the parameters on the interaction between the oscillatory flow and the circular cylinder in the transverse direction are discussed in the following text.

1. Vibration and Vortex Pattern

Figs. 10 and 11 present the time histories and the vortex pat-

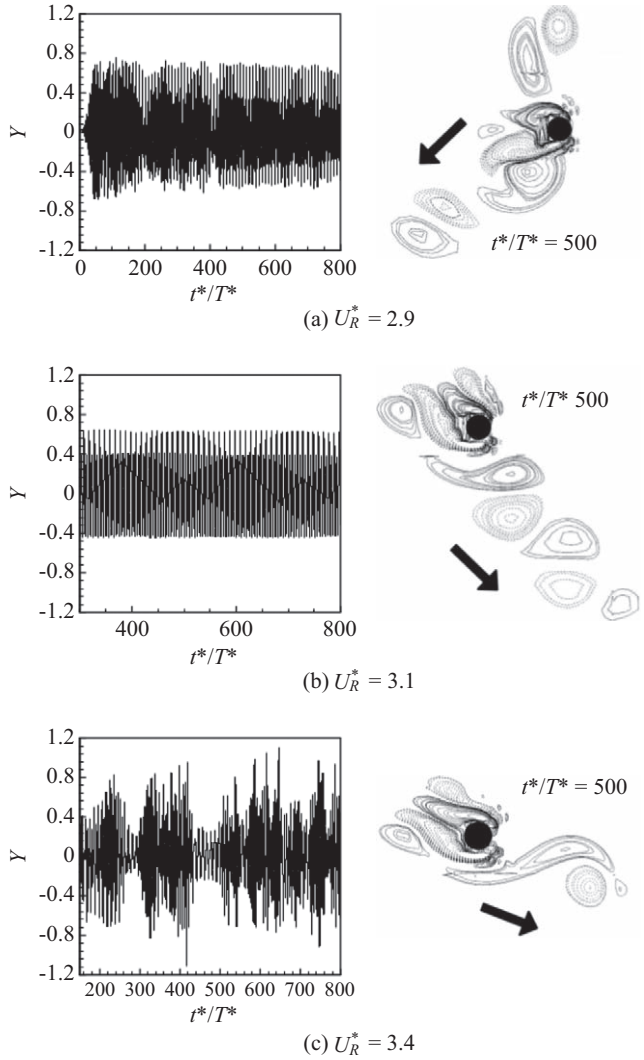

Fig. 10. Cylinder nondimensional transverse displacement y_c^* of y_c/D time series and vortex shedding modes of the vibrating cylinder for various values of reduced velocities at m^* = 1.

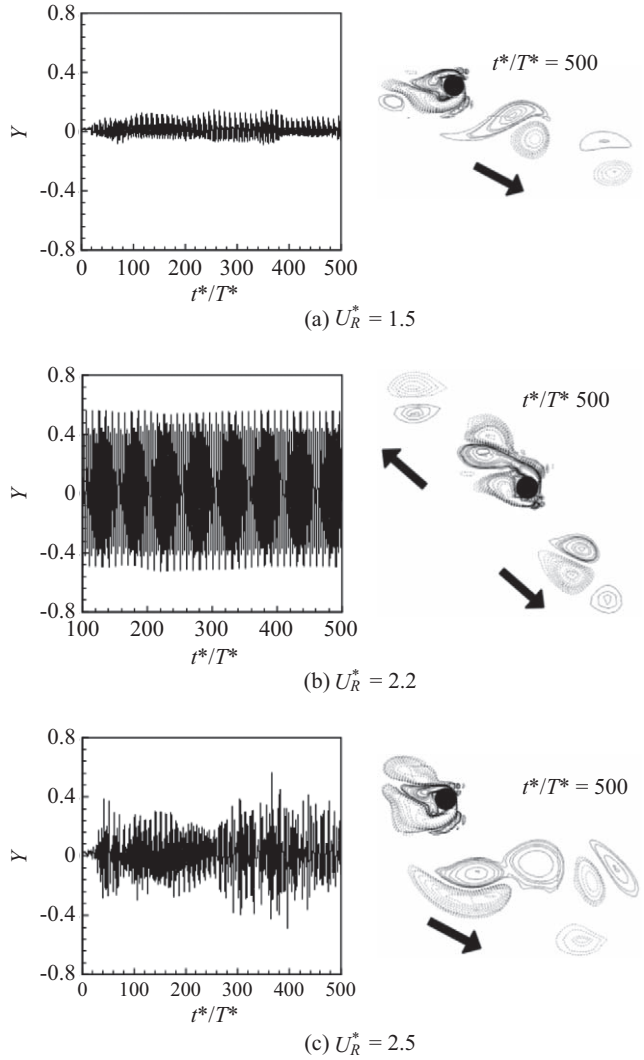

Fig. 11. Cylinder nondimensional transverse displacement $y_c^* = y_c/D$ time series and vortex shedding modes of the vibrating cylinder for various values of reduced velocities at m^* = 1.

terns for a mass ratio m^* of 1 and 1.5, respectively, in the lower (Figs. 10(a) and 11(a)) and higher (Figs. 10(c) and 11(c)) beating and lock-in regions (Figs. 10(b) and 11(b)). When the reduced velocity U_R^* was located near the lock-in region, the cylinder response contained small amplitudes of vibration frequency, and beating patterns (high/low) can be found in this region. Although the vibration of frequency harmonics was regular and repeating for $U_R^* = 2.9$, a clear view of the high beating phenomenon was observed for $U_R^* = 3.4$. The same scenario can be seen in Fig. 11(c) for the following parameter values: $U_R^* = 2.5$ and $m^* = 1.5$. However, in Fig. 11(a) for $U_R^* = 1.5$ and $m^* = 1.5$, a low beating phenomenon was observed with a vibration amplitude of 0.1. Therefore, it is clear from the Figs. 10 and 11 that the high beating phenomenon only occurred after the lock-in region. Moreover, when the reduced velocity was within the lock-in region, the cylinder experienced a large amplitude of vibration. Thus, the lock-in region was based on the reduced velocity U_R^*. From the vortex flow pattern presented in Fig. 10(a), the cycle had a clockwise motion of P vortices that shed downward in a weak and diagonal manner from the left side of the cylinder, thus forcing the cylinder slightly upward (details of vortices patterns mentioned in Williamson and Roshko, 1988). Fig. 10(c) presents an elongated anticlockwise vortex shedding downward in a weak and diagonal manner from the right side of the cylinder with the P vortex mode, thus forcing the cylinder slightly upward. A single (S) vertex mode was found to shed from the left side of the cylinder and moved to the top of the cylinder. From Fig. 11(a), an anticlockwise vortex motion that sheds downward in a weak and diagonal manner from the right side of the cylinder with the 2P vortex mode was observed, thus forcing the cylinder slightly downward. Fig. 11(c) displays an anticlockwise vortex motion. Here, the P mode vortices shed

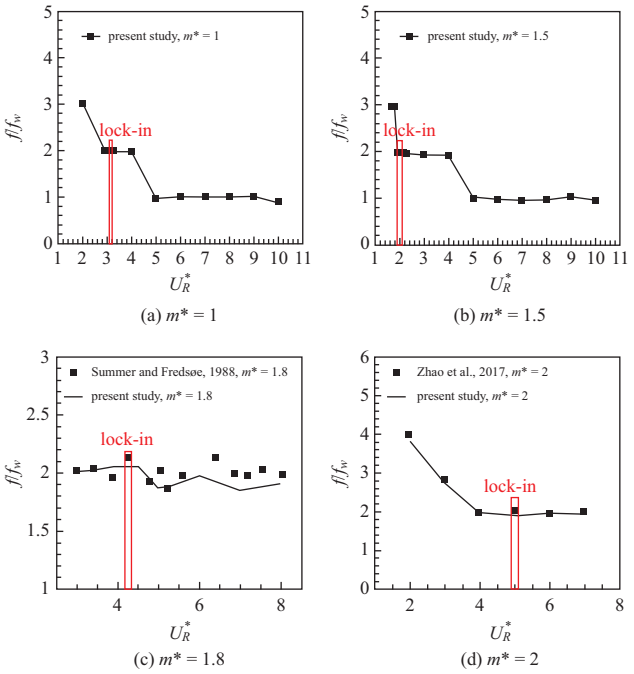

Fig. 12. Variation of the frequency response with reduced velocity.

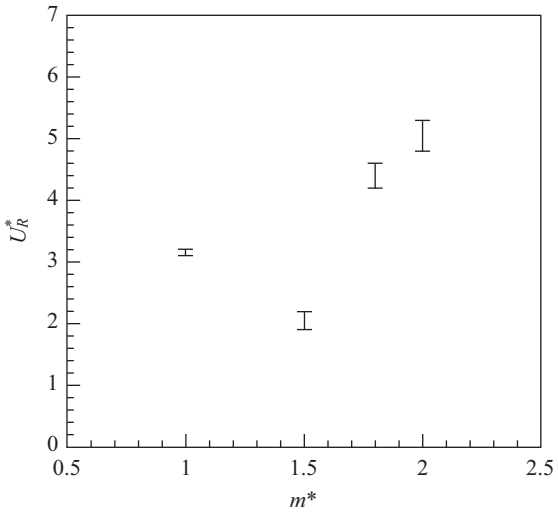

Fig. 13. Frequency response in the lock-in region with varying mass ratio *m.**

downward in a weak and diagonal manner from the right side of the cylinder, thus forcing the cylinder slightly upward.

2. Lock-In Phenomenon

The lock-in phenomenon, or synchronization, means the frequency of structural vibration is similar to the natural frequency. The amplitude of the transverse displacement of the vibrating cylinder reaches up to 0.4 for both reduced velocity U_R^* values of 3.1 and 2.2 in Figs. 10(b) and 11(b), respectively. The lock-in phenomenon occurs for these values of reduced velocity because the vibration profile here is regular and periodic. The vortex pattern visualization displays the occurrence of the 2P vortex shedding mode for each cycle in the lock-in region. The 2P mode vortices moved diagonally downwards in the right side of the cylinder for $U_R^* = 3.1$ and $m^* = 1$ at $t^*/T = 500$, as can be seen in Fig. 10(b). The anticlockwise vortices moved downwards to the bottom of the cylinder, thus forcing the cylinder slightly upward. The vortex pattern in the lock-in region for $U_R^* = 2.2$ and $m^* = 1.5$ at t^*/T of 500 in Fig. 11(b) also appears as the 2P vortex mode and shed diagonally both upward and downward in the cylinder. The pair of vortices moved upward and downward in an anticlockwise direction in the cylinder and shed diagonally from the left and right side of the cylinder, respectively, thus forcing the cylinder slightly downward. In this study, this type of 45° diagonal motion of the vortex shedding could only be seen for the lock-in regions.

3. Frequency Response

The mass ratio m^* varied from 1 to 5. The lock-in phenomenon was successfully captured only for $m^* = 1$, 1.5, 1.8, and 2.0, as presented in Fig. 12. However, the springing phenomenon was recorded appropriately for a higher value of reduced velocity for each value m^* that varied from 1 to 5. From Fig. 12, it can be seen that the fundamental frequency response was maintained at 2 for all m^* values, because the reduced velocity U_R^* was lower than 5. However, when the reduced velocity was greater than 5, the vibration of the cylinder was not influenced by vortex shedding, and the cylindrical vibration was the same as the oscillatory flow. The results of Sumer and Fredsøe (1988) and Zhao et al. (2017) concerning the variation in the frequency response with a reduced velocity at $m^* = 1.8$ and 2.0 were used to validate the results of the present study, demonstrating reasonable agreement.

In addition, as the mass ratio m^* increased from 1 to 2, the region of the lock-in became wider (Fig. 13).

4. Springing Phenomenon

For the VIV on a circular cylinder in a uniform flow, the lock-in region always has the maximum amplitude but different oscillatory flows. From the time history when the U_R^* value was 8 at an $m^* = 1$, a sudden appearance of a rapid rise-and-fall vibration whose maximum amplitude value was double or triple the lock-in amplitude can be observed, as displayed in Fig. 14(a). This type of occasionally occurring transient vibration is known as "springing." The same phenomenon can be observed for $U_R^* = 7$ at m = 1.5, as presented in Fig. 14(b). Gurley and Kareem (1998) reported that springing is due to the second-order wave effect at sum frequencies. When springing occurs, the vortices that appear near the cylinder are bounded around the cylinder. This type of vortex pattern is termed "bound vortex" motion. In the present study, the vortices moved in a clockwise manner around the cylinder, and the cylinder moved downwards, as in Fig. 14(a). The vortices bulged around the cylinder and affected the structure through destruction. The bound vortex formation

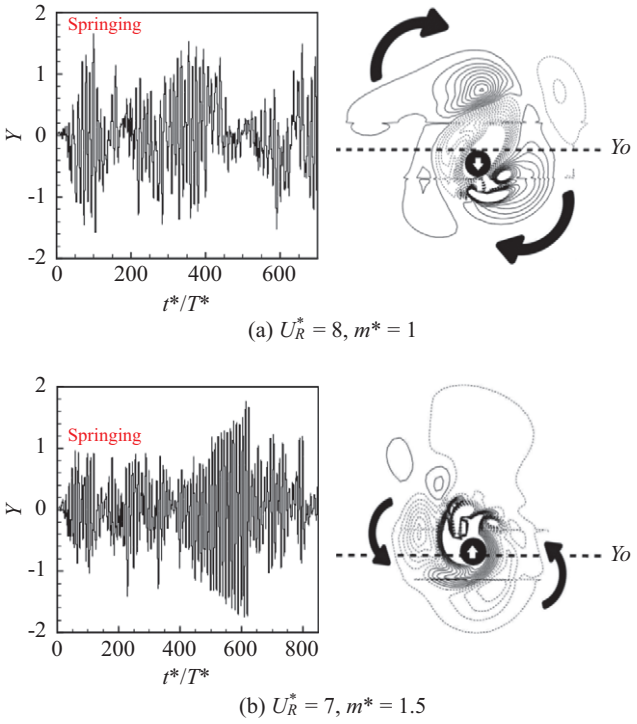

Fig. 14. Time series and vortex shedding modes for a sudden increase in shock.

can also be seen for $U_R^* = 7$ at $m^* = 1.5$, as in Fig. 14(b). Here, the bound vortices moved around the cylinder in an anticlockwise motion as the cylinder moved upward.

5. System Characteristic Diagram

Fig. 15 presents the map of various vortex flow regimes for the transverse vibrating cylinder in an oscillatory flow. These flow regimes are visualized for various mass ratios m^* and reduced velocities U_R^*. The vortex shedding mode in this figure seems to comprise P, S, P + S, and 2P vortex modes. These modes of vortex patterns were clearly defined and presented by Williamson and Roshko (1988). Moreover, the regions marked with S, 2S, P, 2P, and P + S—referred to as the "single vortex," "two single vortices," "single pair," "double pair," and "vortex pair and single vortex," respectively—are shed in each cycle. In this study, all vortex modes found within the lock-in region for different mass ratios were 2P. The S vortex mode was found for a reduced velocity $U_R^* = 5$, 6 and 7 at a mass ratio $m^* = 1.5$. The different vortex mode regions are separated by the lines displayed in Fig. 15 because all the results were successfully obtained for each U_R^* value in the range of 1-10. For a higher value of reduced velocity, the vortex modes were found to be complex and staggered, known as "bound" vortices that were explained and discussed in an earlier section. A springing phenomenon was observed in this study. This phenomenon may be one of the reasons for the formation of bound vortices. The occurrence of springing and bound vortices and their effect on the structure was previously mentioned.

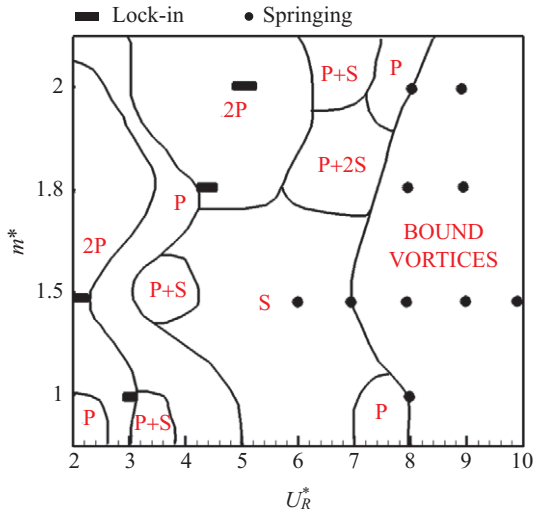

Fig. 15. Vortex shedding modes at each mass ratio.

IV. CONCLUSIONS

DFIB modeling of a vibrating cylinder moving in a transverse direction in an oscillatory flow was conducted. The reduced velocity U_R^* and mass ratio m^* were methodically varied, and their influence on the flow characteristics and cylinder response were investigated. The reduced velocity and mass ratio are crucial factors in the cylinder response of complex VIV problems. When the reduced velocity was located close to the lock-in region, the cylinder response exhibited a small amplitude vibration, and the beating pattern could be found in this region. Moreover, when the reduced velocity was within the lock-in region, the cylinder exhibited a large amplitude oscillation and high hydrodynamic force. The lock-in range of the 2P vortex shedding mode was almost identical. A crucial phenomenon known as "springing" was also noted. This phenomenon is more severe than the lock-in phenomenon because it appears suddenly and leads to structural damage. A vortex pattern of sticking and bounding was found around the cylinder and termed the "bound vortex." The general trend of the lock-in, springing, and vortex shedding modes and their conditions were predicted appropriately.

V. NOMENCLATURE

English Symbols

A: amplitude of vibration, (m)
A^*: dimensionless amplitude, $\frac{A}{D}$
C_L: transverse force coefficient, $-2F_y$
c: structural damping ($N \cdot s \cdot m^{-1}$)
d_y: displacement of cylinder center in y-direction
D: dimensionless diameter of cylinder
F: total dimensionless virtual force
f: response frequency of oscillating cylinder

f_n: solid body natural frequency, $\frac{1}{2\pi}\sqrt{\frac{k}{m_s}}$

f_w: frequency of oscillatory flow

f*: dimensionless virtual force per unit mass, $\frac{fD}{U_\infty^2}$

k: structural stiffness ($N \cdot m^{-1}$)

KC: Keulegan-Carpenter number, $\frac{U_\infty T^*}{D}$

m^*: dimensionless mass ratio, $\frac{4m_s}{\pi\rho_f D^2}$

m_s: structural mass of solid, (kg)

N: number of sub-grid cells

p: dimensionless pressure

R: dimensionless radius of cylinder

Re: Reynolds number, $\frac{U_\infty D}{v}$

T: period of oscillatory flow, (s)

T^*: dimensionless period of oscillatory flow, $\frac{TU_\infty}{D}$

t: time, (s)

t^*: dimensionless time, $\frac{tU_\infty}{D}$

$\mathbf{u}(u, v)$: dimensionless velocity of fluid

$\mathbf{u}'$: dimensionless first intermediate velocity

$\mathbf{u}''$: dimensionless second intermediate velocity

U_∞: free stream velocity, ($m \cdot s^{-1}$)

U_R^*: dimensionless reduced velocity, $\frac{U_\infty}{f_n D}$

x, y: dimensionless Cartesian coordinates

Y: dimensionless displacement, $\frac{a_y}{D}$

Greek Symbols

η: the volume of solid function

v: kinematic viscosity of fluid, ($m^2 \cdot s^{-1}$)

ξ: refinement of sub-grids

ζ: dimensionless damping ratio of structure, $\frac{c}{2\sqrt{m_s k}}$

ρ: density, ($kg \cdot m^{-3}$)

Ω: domain

Subscripts

f: fluid

s: solid

i, j, k, l: numerical cell indices

Superscripts

n: time step level

*: dimensionless parameter

′: first intermediate time step level

″: second intermediate time step level

ACKNOWLEDGEMENTS

The authors would like to express their gratitude for the financial support from the Ministry of Science and Technology, Taiwan (Grant No: MOST 103-2212-E-011-110-MY3 and MOST 106-2221-E-011-079).

REFERENCES

Chern, M. J., W. C. Shiu and T. L. Horng (2013). Immersed boundary modeling for interaction of oscillatory flow with cylinder array under effects of flow direction and cylinder arrangement. Journal of Fluids and Structures 43, 325-346.

Chern, M. J., Y. H. Kuan, G. Nugroho, G. T. Lu and T. L. Horng (2014). Direct-forcing immersed boundary modeling of vortex-induced vibration of a circular cylinder. Journal of Wind Engineering and Industrial Aerodynamics 134, 109-121.

Chern, M. J., D. Z. Noor, C. B. Liao and T. L. Horng (2015). Direct-Forcing Immersed Boundary Method for Mixed Heat Transfer. Communications in Computational Physics 18(4), 1072-1094.

Chern, M. J., E. A. Odhiambo, T. L. Horng and A. G. L. Borthwick (2016). Numerical simulation of vibration of horizontal cylinder induced by progressive waves. Fluid Dynamics Research 48, Article ID 015508.

Chorin, A. J. (1967). The numerical solution of the Navier-Stokes equations for an incompressible fluid. Bulletin of the American Mathematical Society 73(6), 928-931.

Dütsch, H., F. Durst, S. Becker and H. Lienhart (1998). Low-Reynolds-number flow around an oscillating circular cylinder at low Keulegan Carpenter numbers. Journal of Fluid Mechanics 360, 249-271.

Fu, S., J. Wang, R. Baarholm, J. Wu and C. M. Larsen (2014). Features of vortex-induced vibration in oscillatory flow. Journal of Offshore Mechanics and Arctic Engineering 136, Article ID 011801.

Gurley, K. R. and A. Kareem (1998). Simulation of ringing in offshore systems under viscous loads. Journal of Engineering Mechanics 124(5), 582-586.

Hirt, C., B. Nickols and N. Romero (1975). SOLA-A numerical solution algorithm for transient fluid. LA-5852. Los Alamos Scientific Laboratory, Los Alamos, New Mexico, USA.

Kozakiewicz, A., B. M. Sumer and J. Fredsøe (1992). Spanwise correlation on a wall in oscillatory flows. Journal of Fluids and Structures 6, 371-392.

Kozakiewicz, A., B. M. Sumer, J. Fredsoe and E. A. Hansen (1997). Vortex regimes around a freely vibrating cylinder in oscillatory flow. International Journal of Offshore and Polar Engineering 7(2), 94-103.

Leonard, B. P. (1979). A stable and accurate convective modelling procedure based on quadratic upstream interpolation. Computer Methods in Applied Mechanics and Engineering 19, 59-98.

Leontini, J. S., M. C. Thompson and K. Hourigan (2006). The beginning of branching behavior of vortex-induced vibration during two-dimensional flow. Journal of Fluids and Structures 22, 857-864.

Mohd. Yusof, J. (1996). Interaction of massive particles with turbulence. Ph.D. thesis, Cornell University, USA.

Shen, L. W., E. S. Chan and P. Z. Lin (2009). Calculation of hydrodynamic forces acting on a submerged moving object using immersed boundary method. Computers and Fluids 38, 691-702.

Sotiropoulos, F. and X. Yang (2014). Immersed boundary methods for simulating fluid-structure interaction. Progress in Aerospace Sciences 65, 1-21.

Sumer, B. M. and J. Fredsøe (1988). Transverse vibrations of an elastically mounted cylinder exposed to an oscillating flow. Journal of Offshore Mechanics and Arctic Engineering 110, 387-394.

Thorsen, M. J., S. Sævik and C. M. Larsen (2016). Time domain simulation of vortex-induced vibrations in stationary and oscillating flows. Journal of Fluids and Structures 61, 1-19.

Williamson, C. H. K. (1985). Sinusoidal flow relative to circular cylinder. Journal of Fluid Mechanics 155, 141-174.

Williamson, C. H. K. and A. Roshko (1988). Vortex formation in the wake of an oscillating cylinder. Journal of Fluids and Structures 2, 355-381.

Yang, B., F. Gao, D. S. Jeng and Y. Wu (2009). Experimental study of vortex-induced vibrations of a cylinder near a rigid plane boundary in steady flow. Acta Mechanica Sinica 25(1), 51-63.

Zhao, M., L. Cheng and H. An (2012). Numerical investigation of vortex-induced vibration of a circular cylinder in transverse direction in oscillatory flow. Ocean Engineering 41, 39-52.

Zhao, M., K. Kaja, Y. Xiang and G. Yan (2013). Vortex-induced vibration (VIV) of a circular cylinder in combined steady and oscillatory flow. Ocean Engineering 73, 83-95.

Zhao, M., T. Pearcey, L. Cheng and Y. Xiang (2017). Three-Dimensional Numerical Simulations of Vortex-Induced Vibrations of a Circular Cylinder in Oscillatory Flow. Journal of Waterway, Port, Coastal, and Ocean Engineering 143(4), 04017007.